Materials & Design 252 (2025) 113800

Contents lists available at ScienceDirect

Materials & Design

journal homepage: www.elsevier.com/locate/matdes

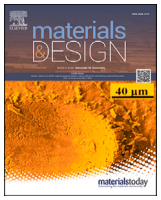

Spring-based mechanical metamaterials with deep-learning-accelerated design

Xiaofeng Guo [a], Xiaoyang Zheng [b,*], Jiaxin Zhou [c,d], Takayuki Yamada [b], Yong Yi [a,*], Ikumu Watanabe [c,d,*]

[a] School of Materials Science and Engineering, Southwest University of Science and Technology, Mianyang 621010, China
[b] Institute of Engineering Innovation, Graduate School of Engineering, The University of Tokyo, Tokyo 113-8656, Japan
[c] Graduate School of Pure and Applied Sciences, University of Tsukuba, 1-1-1 Tennodai, Tsukuba 305-8573, Japan
[d] Center for Basic Research on Materials, National Institute for Materials Science, 1-2-1 Sengen, Tsukuba 305-0047, Japan

ARTICLE INFO

Keywords:
Mechanical metamaterial
Deep learning
Inverse design
Soft robotics
Flexibility

ABSTRACT

Mechanical metamaterials exhibit unique properties that depend on their microstructure and surpass those of their constituent materials. Flexible mechanical metamaterials, in particular, hold significant potential for applications requiring substantial deformations, such as soft robotics and energy absorption. In this study, we proposed a collection of flexible mechanical metamaterials discretely assembled using structural spring elements. These spring elements enhance both flexibility and reversibility, allowing the materials to withstand large deformations. The geometric regularity of the metamaterials enables zero-shot learning, allowing deep learning frameworks to address property prediction and inverse design problems beyond the training dataset. Using a property-prediction model, the effective mechanical properties of these metamaterials can be accurately predicted based on specified design parameters. Furthermore, an inverse-design model enables the direct generation of mechanical metamaterials with desired target properties, even outside the training dataspace, in the range of Young's modulus $E \in (0, 350)$ kPa and Poisson's ratio $\nu \in (-0.12, 0.12)$. The properties of these inversely designed metamaterials are analyzed through finite element method simulations and mechanical testing. The deep learning-accelerated design approach not only streamlines the development process but also provides a framework for advancing metamaterial design, encompassing property prediction and inverse design.

1. Introduction

Mechanical metamaterials, typically composed of periodic buckling blocks, are artificially architected materials with exceptional mechanical properties that arise from the spatial arrangement of their geometric elements [1,2]. These materials are capable of exhibiting exceptional properties and functionalities that not only differ from but often surpass those of their constituent materials. Notable examples include metamaterials with negative Poisson's ratios [3–5], a high stiffness-to-density ratio [6], negative stiffness [7,8], variable stiffness [9,10], and reprogrammable mechanical responses [11,12]. These unique properties make mechanical metamaterials ideal for a wide range of applications, including actuators [13], dampers [14], soft robotics [12], energy absorption [15,16], buffer devices [17], and wearables [18].

In particular, flexible mechanical metamaterials demonstrate significant potential in applications requiring both flexibility and resilience, such as soft robotics and energy absorption [12,15,16,19–21]. These materials can undergo large reversible deformations without experiencing structural or material failure. However, traditional mechanical metamaterial designs frequently rely heavily on the softness of their constituent materials, such as rubber-like materials [12,22,23]. The hyperelasticity of these materials enables metamaterials' recovery after external loads are removed, but this softness also limits the range of achievable stiffness, even at high relative densities. Additionally, although some studies have investigated the use of structural instabilities (e.g., buckling) to achieve reversible deformation, the slenderness of the buckling beams restricts the variation in stiffness [5,24]. This limitation stems from the linear buckling behavior of the beams, which inherently results in a reduction in stiffness or, in some cases, in unrecoverable plastic deformation.

* Corresponding authors.
E-mail addresses: xzheng@g.ecc.u-tokyo.ac.jp (X. Zheng), yiyong@swust.edu.cn (Y. Yi), WATANABE.Ikumu@nims.go.jp (I. Watanabe).

https://doi.org/10.1016/j.matdes.2025.113800
Received 21 November 2024; Received in revised form 14 February 2025; Accepted 3 March 2025

Available online 6 March 2025

Moreover, mechanical metamaterials are commonly fabricated using advanced additive manufacturing technologies [25–27]. While these advancements have revolutionized the fabrication of continuous, monolithic structures and enabled the creation of multiscale and multimaterial designs from a variety of materials, challenges remain in printing complex metamaterials. For example, achieving intricate interior morphologies and immaculate surface finishes is still difficult. Air bubbles often form within the chambers of metamaterials during the additive manufacturing process, resulting in the emergence of structural defects [28]. An alternative approach to overcome these limitations involves constructing metamaterials through the discrete assembly of a finite set of parts [29–31]. By printing individual structural elements with intricate features separately and assembling them afterward, manufacturers can circumvent some of the constraints of current machines. This modular assembly method facilitates the spatial composition of diverse properties, including rigidity, compliance, chirality, and auxetic behavior [29]. Moreover, this approach is particularly beneficial for modular robotics, where various modules and components can be combined to create flexible and customized automation solutions [32–34].

Additionally, traditional design strategies for mechanical metamaterials typically follow a forward-design approach, where the design space and outcomes depend on the intuition and experience of designers, often requiring multiple rounds of trial and error. The effective properties of the designed microstructures must then be analyzed through time-consuming computational simulations or experiments. Recent advancements in deep learning have transformed the microstructure design process for materials [1,35]. For instance, the effective properties of metamaterials can now be predicted using deep learning frameworks that incorporate multilayer perceptrons or convolutional neural networks [36]. Furthermore, deep generative models—such as generative adversarial networks, variational autoencoders, diffusion models, and flow-based models—enable the generation of microstructures with optimized properties [37–39]. More importantly, with additional modules, these deep generative models enable inverse design, allowing for the autonomous generation of metamaterials with targeted properties and functions [40–44]. The inverse design process eliminates the reliance on designer intuition and removes the inefficient trial-and-error methods. The training data for inverse design consists of labeled geometric representations, which can be either implicit—such as modeling parameters and numerical descriptions of geometric elements—or explicit—such as pixels (images), voxels, point clouds, or meshes [1]. These deep learning algorithms significantly accelerate the metamaterial design process.

In this study, we propose a novel class of spring-based mechanical metamaterials integrated with deep learning-accelerated design frameworks. These metamaterials consist of spring elements discretely assembled in various spatial configurations, resulting in diverse structural layouts. The steel spring elements offer superior flexibility and reversibility compared to traditional rubber-like materials. The combination of material selection (e.g., steel), structural element design (spring), and spatial configuration arrangement allows for a wide range of variable stiffness and Poisson's ratios. First, we prepared a labeled dataset consisting of spring-based mechanical metamaterials with various geometric parameters, along with their corresponding Young's moduli and Poisson's ratios. This dataset was used to train two deep learning models: one for property prediction and the other for inverse design. The first model predicts the effective properties of the metamaterials based on the input design parameters, while the second model generates geometric parameters based on desired target properties. We then created contour maps of material properties using the trained property-prediction model to guide functional applications. The geometric regularity of the metamaterials enables zero-shot learning, allowing the inverse-design model to directly generate mechanical metamaterials with desired target properties even outside the training dataspace in the range of Young's modulus $E \in (0, 350)$ kPa and Poisson's ratio $\nu \in (-0.12, 0.12)$. Finally, we generated metamaterials using the trained inverse-design model, evaluated their mechanical properties through testing, and validated the results using finite element method (FEM) simulations.

This study presents two key novelties. First, a novel structural design is presented, integrating steel springs and hollow plastic spherical nodes to construct flexible, resilient metamaterials. While traditional truss lattices are commonly fabricated via 3D printing, which inherently imposes manufacturing constraints, the proposed component-assembly method mitigates limitations related to manufacturing scale and material selection. Second, we leverage deep learning for zero-shot learning, enabling property prediction and inverse design of these metamaterials. This approach diverges from conventional approaches that rely on finite element simulations for predicting effective material properties. The resulting spring-based metamaterials, with their high resilience, reversibility, and flexibility, hold promise across diverse applications, including soft robotics, actuators, energy absorption, and impact protection.

Table 1
Geometric parameters of a spring element.

Geometric parameter	Symbol
Wire Diameter	d (mm)
Outer Diameter	D (mm)
Pitch	p
Effective Number of Turns	n
Free Height	L (mm)
Shear Modulus of a Material	G (MPa)
Working Load	F (N)

2. Methods

2.1. Modeling

Spring-based mechanical metamaterials consist of spring elements arranged in various lattice configurations (Fig. 1). These configurations can be easily assembled, freeing the design from fabrication constraints and allowing for low-cost production of components. In this study, three cubic crystal systems — simple cubic (SC), body-centered cubic (BCC), and face-centered cubic (FCC) — are utilized to construct the building blocks of the metamaterials. The ligaments of each building block are springs, which serve as elastic elements to absorb vibration and shock energy through deformation. A spring is characterized by several design parameters, including wire diameter d, outer diameter D, spring pitch p, number of turns n, and height L, as illustrated in Fig. 2 and detailed in Table 1. The working load F of a spring is calculated as follows:

$$F = \frac{Gd^4}{8nD^3}, \tag{1}$$

where G represents the shear modulus of the constitutive material. By adjusting these design parameters, the stiffness of the spring can be tailored to specific applications.

2.2. Dataset preparation

To prepare a dataset for deep learning training, we generated 801 unique geometries for each of three lattice configurations (SC, BCC, and FCC) by varying the number of turns $n \in [3, 7]$ and outer diameter $D \in [0.8, 1.2]$ mm of spring-based mechanical metamaterials. The inner diameter and pitch were fixed at $d = 0.2$ mm and $p = 0.5$ mm, respectively.

The effective mechanical properties of these metamaterials were calculated using a FEM simulation tool (COMSOL Multiphysics version 6.1, COMSOL, Sweden). This simulation approach has been validated in previous studies [5,9,40,41]. Each metamaterial geometry was modeled using spherical nodes and spring ligaments, combined using a union

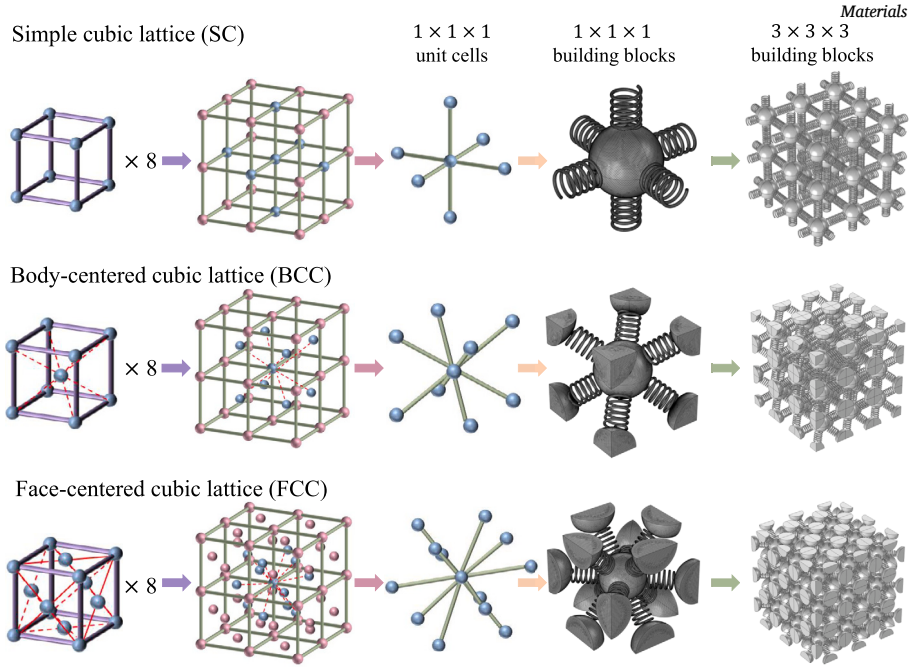

Fig. 1. Concept of spring-based mechanical metamaterials. It illustrates three cubic lattice configurations, each composed of spring elements and spherical nodes.

operation. Fig. 1 shows examples of the finite element meshes. All simulations were conducted on a $1 \times 1 \times 1$ building block under periodic boundary conditions, following the finite element analysis method for a representative volume element (RVE) [45,46]. A perturbation periodic displacement field was solved for a prescribed macroscopic strain or stress mode.

An isotropic elastoplastic constitutive model based on the von Mises yield criterion was employed in the simulations. As the stress levels were expected to remain below the yield strength, plastic hardening was neglected. The spring elements were modeled as 304 stainless steel (Young's modulus $E = 193$ GPa, Poisson's ratio $\nu = 0.3$, yield strength $\sigma_Y = 205$ MPa), while the spherical nodes were modeled as a 3D-printed plastic ($E = 2.6$ GPa, $\nu = 0.4$, $\sigma_Y = 40$ MPa). Due to the low density of the hollow microstructures, self-weight effects were neglected in the simulations. Macroscopic uniaxial stress was applied to an RVE until a compressive engineering strain of $\varepsilon = 0.1$ was reached. The macroscopic Young's modulus and Poisson's ratio were subsequently calculated from the resulting macroscopic stress–strain curve and the transverse and longitudinal components of the macroscopic strain.

The dataset consists of $N = 2403$ data points, corresponding to 801 geometries for each of the three lattice configurations. Each data point includes a geometric representation (outer diameter D, turn number n, and lattice configuration η) and corresponding mechanical properties (Young's modulus E and Poisson's ratio ν) in the form of $S = \{(D_i, n_i, \eta_i), (E_i, \nu_i)\}_{i=1}^{N}$. Fig. 3 visualizes the distribution of the mechanical properties in the dataset, showing coverage over a quadrilateral region.

Note that the Young's moduli were normalized by the spring's Young's modulus during deep learning training. This normalization allows the trained deep learning models to generalize to different spring materials, enabling accurate predictions for a wide range of design parameters. The standard basis was used to define the lattice configuration: SC (1, 0, 0), BCC (0, 1, 0), and FCC (0, 0, 1).

2.3. Deep learning framework construction

We developed two deep learning frameworks to utilize the generated dataset for property prediction and inverse design, respectively. Both frameworks share the same hidden layers, consisting of four fully connected layers with ReLU activation functions, featuring 1024, 2048, 4096, and 2048 units, respectively (Fig. 4a). For the property-prediction framework (f), the model was trained to predict the effective mechanical properties based on the design parameters, expressed as $(\hat{E}, \hat{\nu}) = f(D, n, \eta)$. The mean absolute error (MAE) was utilized as the loss function to compare the predicted values with the reference values:

$$\mathcal{L}_f = \frac{1}{N} \sum_{i=1}^{n} \left((E_i, \nu_i) - (\hat{E}_i, \hat{\nu}_i) \right)^2 \tag{2}$$

For the inverse design framework (g), the model was trained to predict the design parameters based on the target properties, expressed as $(\hat{D}, \hat{n}, \hat{\eta}) = g(E, \nu)$. The loss function was calculated using the MAE:

$$\mathcal{L}_g = \frac{1}{N} \sum_{i=1}^{n} \left((D_i, n_i, \eta_i) - (\hat{D}_i, \hat{N}_i, \hat{\eta}_i) \right)^2 \tag{3}$$

The deep learning frameworks were trained using TensorFlow (version 2.12.0) on a single NVIDIA RTX A6000 graphics card (48 GB GPU memory) within a Linux environment. Python 3.10 and CUDA 11.8 were used for the implementation. The model was trained using the Adam optimizer with a learning rate of 0.0001. Training for 200 epochs took approximately 1 minute, while 500 epochs took around 2 minutes on

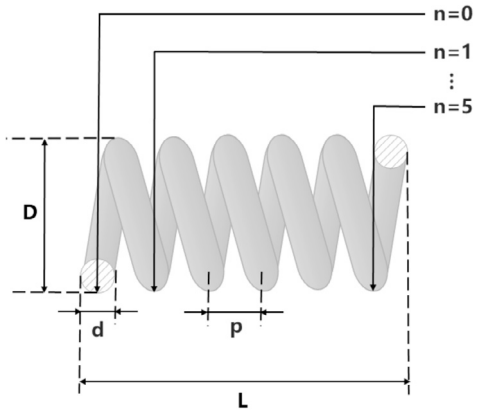

Fig. 2. Design parameters of the spring element.

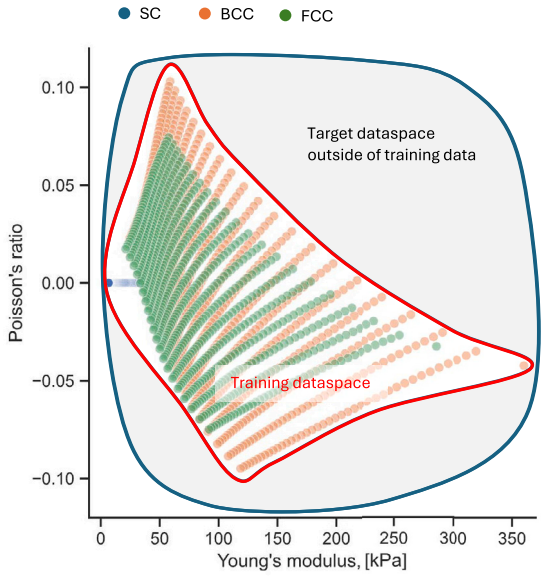

Fig. 3. Training dataset map generated with different design parameters. The training dataspace covers a quadrilateral pattern within the red outline, and target dataspace outside of the training dataspace is used for inverse design.

the NVIDIA RTX A6000. The $N = 2403$ data points were split into training and validation sets with a ratio of 0.8:0.2.

2.4. Mechanical testing

Prototypes of spring-based metamaterials were assembled using 3D-printed hollow plastic spherical nodes and commercially available steel springs. The use of plastic spheres reduced weight without significantly affecting the overall Young's modulus and Poisson's ratio of the metamaterials. While increasing spring stiffness can elevate the Young's modulus, it has a minimal impact on the Poisson's ratio, which is primarily determined by the structure configuration. Hollow spherical nodes were fabricated using a stereolithography 3D printer (JS-1700, Kings 3D Printing, China) with resin (C-UV 9400E, Elite Intelligent Manufacturing, China). A detailed description of the fabrication method is provided in Section 3.2.

The mechanical properties of the fabricated metamaterials were evaluated through uniaxial compression tests performed on a motorized test stand (AGXplus-10kN, Shimadzu, Japan). The samples were placed directly onto the compression platform, with their bottom surfaces unconstrained. Strain-rate-dependent compression tests were conducted at deformation rates of 0.5 mm/min, 5 mm/min, and 50 mm/min, with a stopping criterion defined as a compressive strain of 0.1. High-speed cameras recorded the deformation process from both front and side perspectives. Stress–strain curves were generated from the recorded load and displacement data.

3. Results and discussion

3.1. Property prediction

We initially trained a deep learning framework to predict the properties of spring-based metamaterials. Fig. 4b shows the training loss converging rapidly to 0.01 after 25 epochs, indicating a stable training process. Figs. 4c and d illustrate the framework's performance on validation data. Each scatter point compares the reference and predicted values of effective mechanical properties (Young's modulus and Poisson's ratio). Points closer to the bisection line ($x = y$) represent better predictive performance. Fitting the scatter points to the bisection line yields $R^2 = 0.9987$ for Young's modulus and $R^2 = 0.9954$ for Poisson's ratio. These high R^2 values demonstrate the framework's ability to accurately predict these properties based on given design parameters.

Table 2
Comparison of the FE and ML models using design parameters without training.

Design parameters	FE model	ML model
$D = 0.6, n = 2, \eta$ =SC	$E = 283.25$ kPa, $\nu = 6.532 \times 10^{-6}$	$E = 285.47$ kPa $\nu = 6.301 \times 10^{-7}$
$D = 0.6, n = 2, \eta$ =BCC	$E = 1336.32$ kPa $\nu = -4.986 \times 10^{-2}$	$E = 1334.16$ kPa $\nu = -4.745 \times 10^{-2}$
$D = 0.6, n = 2, \eta$ =FCC	$E = 1056.64$ kPa $\nu = -4.210 \times 10^{-2}$	$E = 1057.25$ kPa $\nu = -3.723 \times 10^{-2}$
$D = 1.4, n = 8, \eta$ =SC	$E = 23.86$ kPa $\nu = 5.785 \times 10^{-6}$	$E = 21.49$ kPa $\nu = 4.712 \times 10^{-8}$
$D = 1.4, n = 8, \eta$ =BCC	$E = 141.54$ kPa $\nu = -1.479 \times 10^{-1}$	$E = 137.79$ kPa $\nu = -1.384 \times 10^{-1}$
$D = 1.4, n = 8, \eta$ =FCC	$E = 112.65$ kPa $\nu = -1.156 \times 10^{-1}$	$E = 113.19$ kPa $\nu = -1.170 \times 10^{-1}$

Given the strong performance of the property-prediction framework, we predicted the effective properties of spring-based metamaterials with varying design parameters, including outer diameter D, number of turns n, and lattice configuration η. Fig. 5a presents the contour maps of Young's moduli for the metamaterials across three different configurations. The results indicate that Young's modulus decreases with increasing D and n for all configurations, which can be attributed to the reduced stiffness of the springs. Notably, the SC configuration exhibits the lowest stiffness for the same values of D and n compared to the other two configurations, likely due to its fewer spring elements and the arrangement of the springs in vertical and horizontal layouts. Fig. 5b displays the contour maps of the Poisson's ratios. In contrast to the trends observed in the Young's modulus maps, the Poisson's ratio maps demonstrate a different pattern in relation to D and n. For the SC configuration, the Poisson's ratio decreases with both D and n; however, for the BCC and FCC configurations, the Poisson's ratio increases with n but decreases with D. Interestingly, the SC configuration exhibits near-zero Poisson's ratios, which can be attributed to the vertical and horizontal arrangement of the spring elements: under compressive loading, the vertical springs compress while the horizontal springs remain unchanged, resulting in negligible transverse strains and consequently vanishing Poisson's ratios.

Given that the properties of mechanical metamaterials are intrinsically linked to their relative density (solid volume fraction), we present the relationship between structural relative density and both Young's modulus and Poisson's ratio in Figs. 5c and d. The results clearly demonstrate that these structures encompass a broad property space, exhibiting a hundredfold variation in stiffness and a transition of Poisson's ratio from negative to positive values, thus highlighting the superior performance of our spring-based metamaterials.

We further investigated the zero-shot learning capabilities of the trained deep learning model, which refers to the ability to correctly perform tasks on new, unseen inputs without explicit training. To assess this, we tested the property-prediction framework using input design parameters that fell outside the range of the training data. Table 2 presents examples of predicted effective mechanical properties, compared with FEM simulation results. The 12 paired values of Young's modulus and Poisson's ratio, derived from design parameters (i.e., $D = \{0.6, 1.4\}, n = \{2, 8\}, \eta = \{\text{SC, BCC, FCC}\}$) that were not included in the training dataset, exhibit good agreement. This demonstrates that the property-prediction framework can accurately predict the effective mechanical properties of spring-based metamaterials using input design parameters beyond the training data range.

This zero-shot learning ability can be attributed to the inherent geometric regularity of the metamaterials, where the Young's modulus and

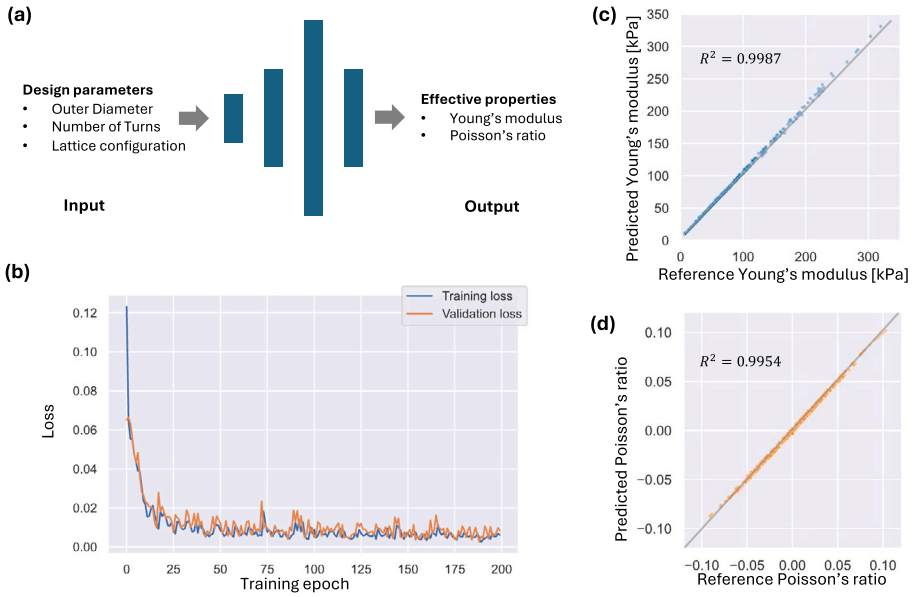

Fig. 4. Deep learning framework for property prediction. (a) Architecture of the property prediction framework. (b) Loss vs. epoch curves of training results. (c) Reference vs. predicted Young's modulus. (d) Reference vs. predicted Poisson's ratio.

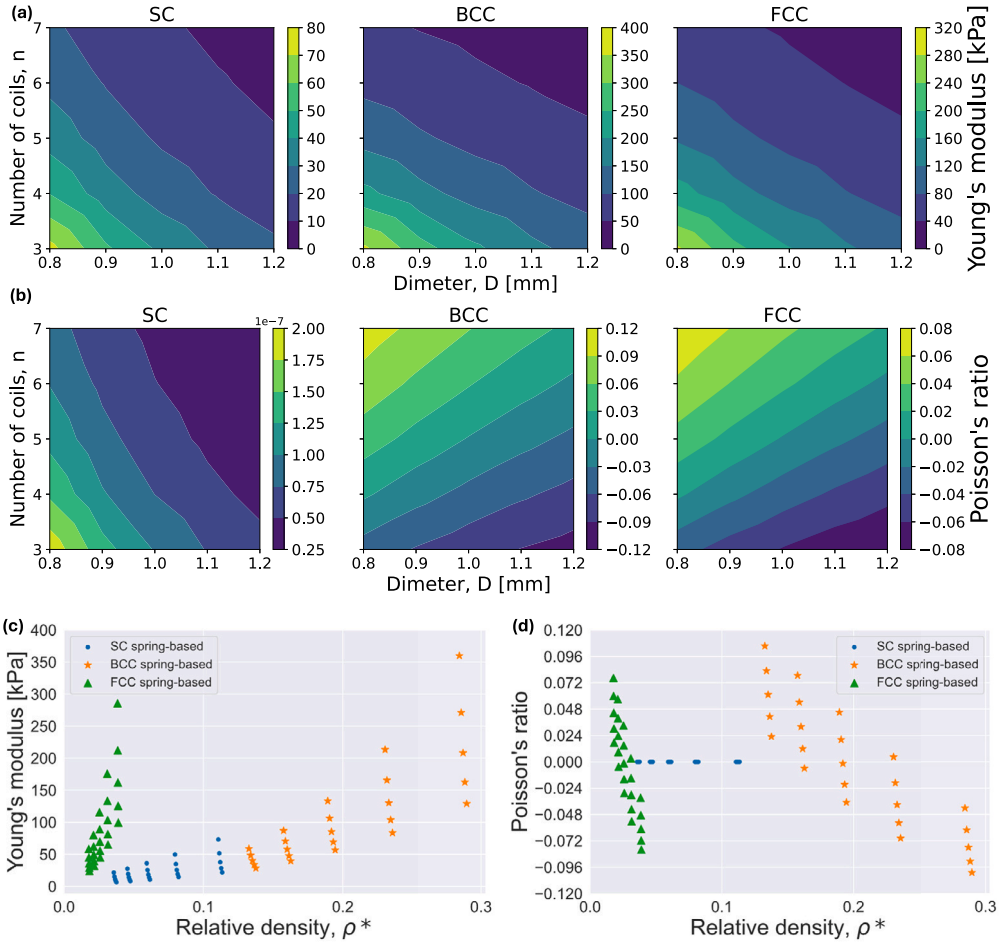

Fig. 5. Relationship between mechanical properties and design parameters for spring-based mechanical metamaterials with different configurations. Contour maps of Young's modulus (a) and Poisson's ratio (b) as a function of spring outer diameter and number of coils. Plots of Young's modulus (c) and Poisson's ratio (d) as a function of relative density (solid volume fraction).

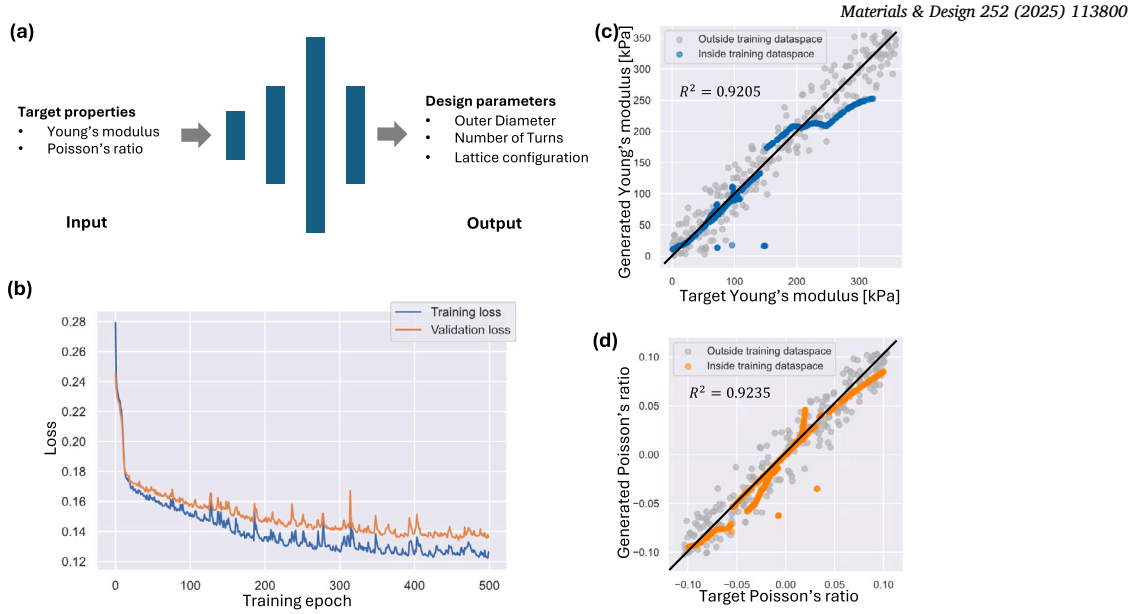

Fig. 6. Deep learning framework for inverse design. (a) Architecture of the inverse design framework. (b) Loss vs. epoch curves of training results. (c) Target vs. generated Young's modulus. (d) Target vs. generated Poisson's ratio.

Poisson's ratio of each lattice configuration are directly proportional to the diameter and number of coils of the spring elements.

3.2. Inverse design

We further trained a deep learning framework for the inverse design of spring-based metamaterials. Fig. 6b shows the training loss converging gradually to 0.13 for training and 0.14 for validation after 300 epochs, indicating a stable training process. Figs. 6c and d illustrate the framework's performance using target properties randomly sampled from both inside and outside of the training dataspace (Fig. 3).

We sampled 512 random E–ν paired values from each dataspace and fitted them to the bisection line using scatter plotting, where each scatter's coordinate corresponds to the target and generated Young's modulus or Poisson's ratio. The result shows that these scatters are well fitted by the bisection line with $R^2 \approx 0.92$, although the scatters from inside the training dataspace are closer to the bisection line compared to those from outside the training dataspace.

It is noteworthy that the inverse design framework can successfully generate spring-based metamaterials with properties outside the training dataspace, as shown by the gray scatters in Figs. 6c and d. This capability is likely due to the inherent geometric regularity of the metamaterials, which makes it easier for the deep learning model to capture the relationship between microstructure and mechanical properties. In contrast, deep-learning-based inverse design frameworks trained on architected materials with disordered microstructures often struggle to generate materials with target properties outside the training dataspace [41]. This suggests that deep learning models can more effectively find the property-microstructure relationship for materials with geometric regularity.

Given that the trained inverse-design framework can generate spring-based metamaterials with specified target properties, we input three distinct sets of target Young's modulus and Poisson's ratio:

$$(E, \nu) = \{(25\ \text{kPa}, 0.), (90\ \text{kPa}, 0.015), (100\ \text{kPa}, 0.02)\}.$$

This yielded three corresponding pairs of design parameters. Using these design parameters, we fabricated metamaterials composed of steel spring elements and 3D-printed hollow spherical nodes, as illustrated in Fig. 7. The spherical nodes and springs were designed for interlocking assembly, with extended spring ends that fit into notches in the spherical nodes. This interlocking design, similar to Lego bricks, ensured precise alignment and minimized human error by defining fixed assembly points and depths for the structural components. To further enhance structural stability, the spherical nodes were designed to be hollow, facilitating direct and secure spring insertion for robust interlocking. Consequently, these metamaterials can be assembled with high precision and exhibit good stability. These structural components were manually assembled using ruler measurements to ensure secure fixation of the components. To ensure structural stability and minimize variations arising from manual assembly, the connection angles of the pins in the spring elements were designed to be constant. Therefore, in the design of the hollow plastic spherical nodes, holes (pins) were incorporated at specified angles, as illustrated in Fig. 7d, to maintain these angles consistently throughout the assembly process. These metamaterials were manually assembled into a configuration of $4\times4\times4$ building blocks, exhibiting negligible deformation due to self-weight. In contrast to full 3D-printed fabrication, this manual assembly approach using commercially available spring elements offers substantial cost and efficiency advantages compared to metallic additive manufacturing. Furthermore, commercial steel spring elements demonstrate superior robustness compared to their 3D-printed counterparts.

We further investigated the mechanical responses of the fabricated metamaterials through uniaxial compressive testing. Figs. 8a, b, and c present a series of progressive deformation configurations derived from both experiments and FEM models for the three metamaterials. While the simulations were performed on RVEs, resulting in idealized deformation states, the experiments were conducted on $4 \times 4 \times 4$ building blocks, leading to heterogeneous deformations due to boundary effects. However, these heterogeneous deformations were not significant, and the results demonstrate good agreement in deformation states between experiments and simulations. The simulated von Mises stress maps indicate that these metamaterials experience relatively low stress, remaining below the yield strengths even when subjected to large deformations of $\varepsilon = 0.1$. For further clarity and quantitative comparison, Fig. 8d presents a direct comparison of the stress–strain curves for the three metamaterials, derived from both experimental measurements and finite element simulations. The observed similarity between the experimentally measured and simulated curves provides additional validation for the robustness of our finite element simulation method.

The resilience of the fabricated metamaterials was evaluated through ten cycles of loading and unloading (Fig. 9). These metamaterials

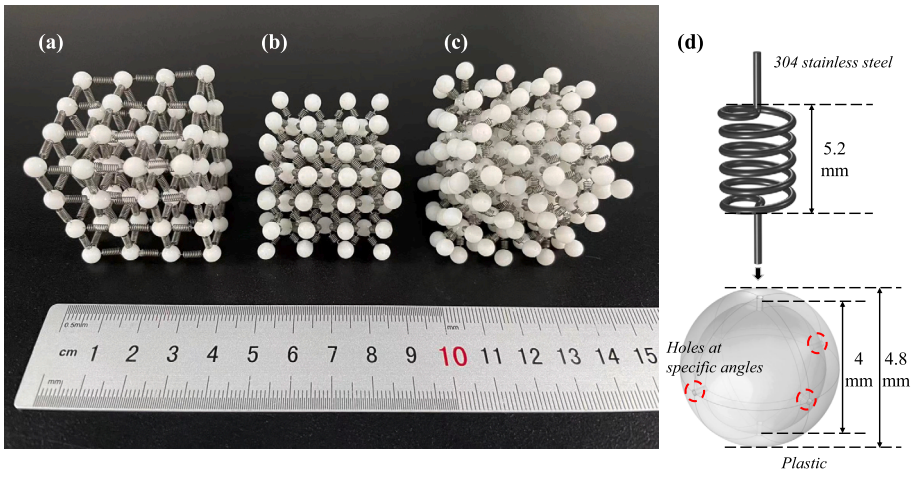

Fig. 7. Prototypes (a) SC, (b) BCC, (c) FCC spring-based mechanical metamaterials, (d) Connection of spring and spherical node.

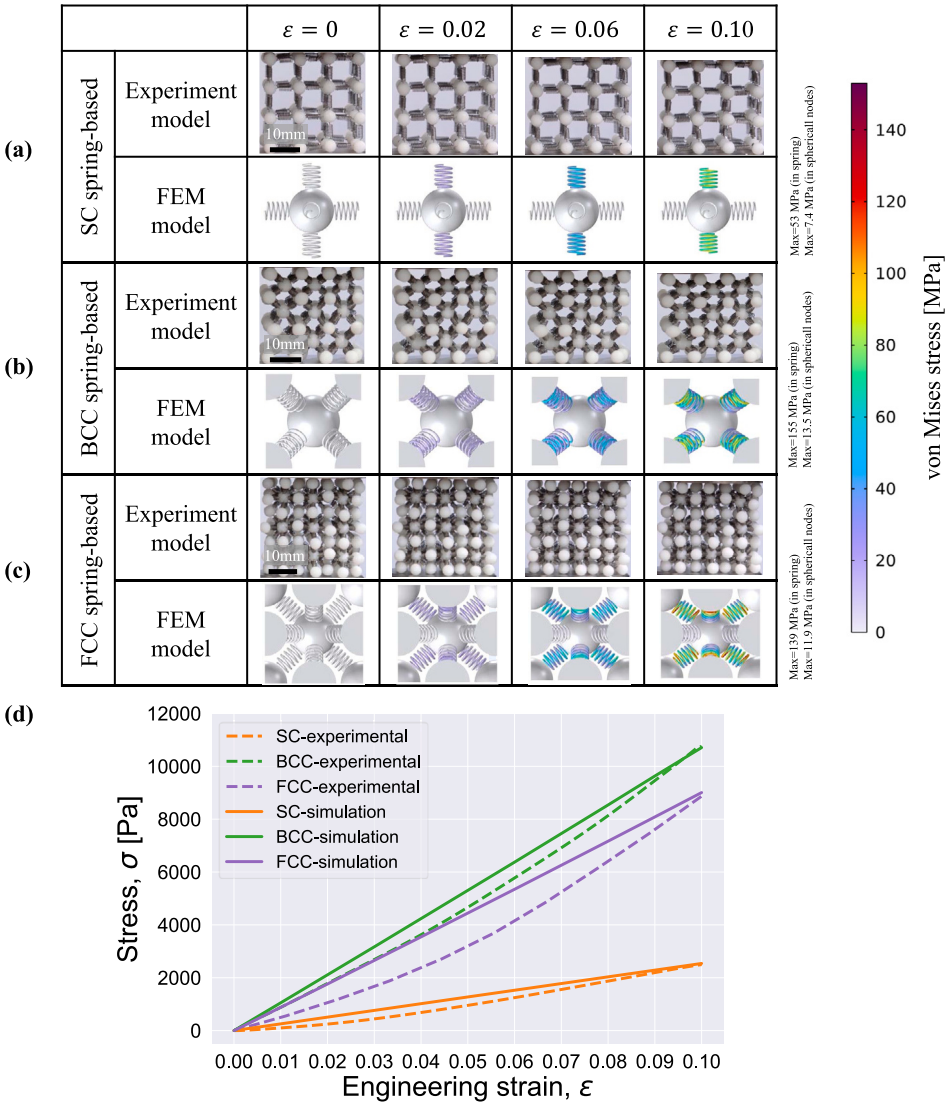

Fig. 8. Mechanical characterization of fabricated metamaterials under uniaxial compression. Deformed configurations from experimental testing and finite element analysis for (a) SC, (b) BCC, and (c) FCC structures. (d) Stress-strain response of the three structures, comparing experimental and numerical results.

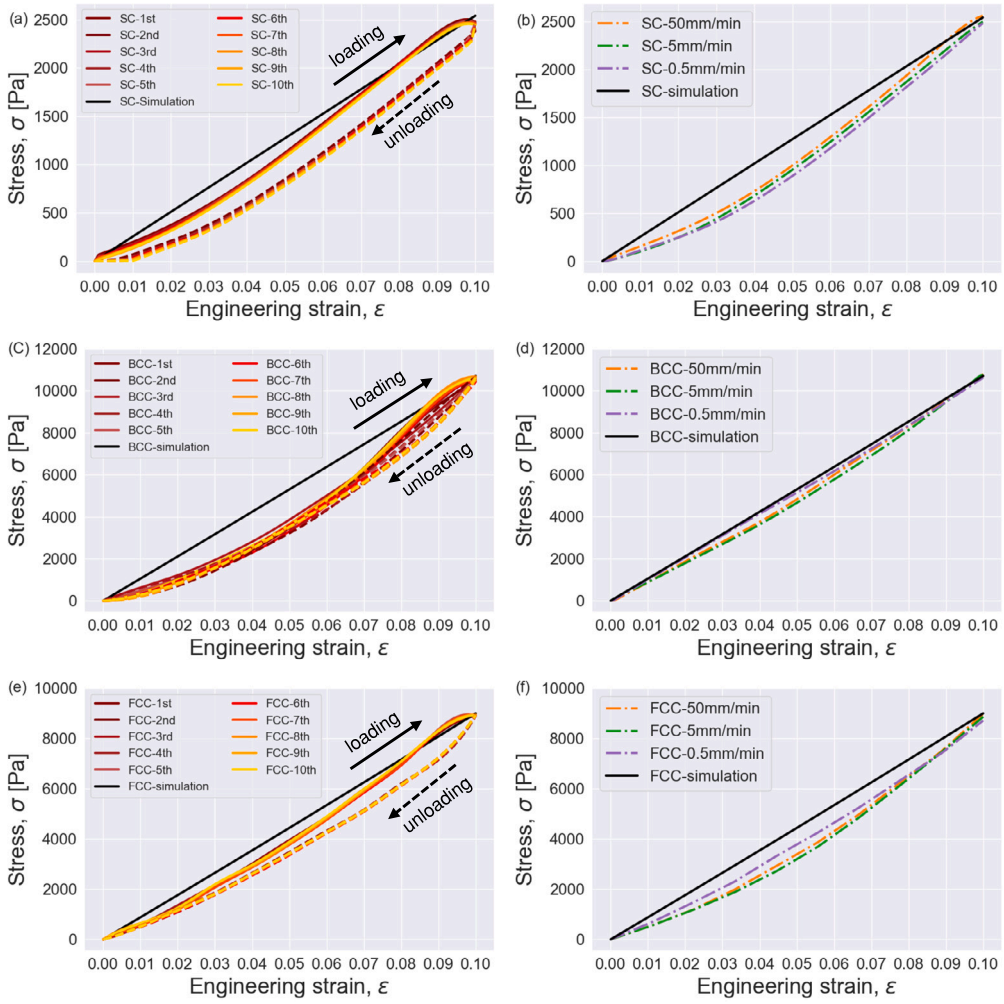

Fig. 9. Stress–strain curves of the fabricated metamaterials from loading-unloading tests (left column) and strain-rate-dependent compressive tests (right column). In left column, solid and dotted lines show loading and unloading curves, respectively. (a,b) SC, (c,d) BCC, and (e,f) FCC configurations.

demonstrated rapid recovery without structural fatigue, even after multiple compression cycles, showcasing their excellent resilience and structural flexibility. To investigate the impact of loading rate, we performed strain-rate-dependent compression tests on these samples (Fig. 9). The results show that the loading rate (i.e., 50 mm/min, 5 mm/min, and 0.5 mm/min) has a minimal effect on the strain–stress curves of the fabricated metamaterials below 50 mm/min, demonstrating their ability to recover immediately upon load removal.

Additionally, the strain–stress curve from the FEM simulation was compared with the experimental curves shown in Fig. 9. The simulated curve is relatively linear, while the experimental curves exhibit a slight exponential increase. This discrepancy can be attributed to experimental errors, such as non-straight deformation of spring elements and partial surface contact during compression. Overall, the results confirm the resilience and reversibility of the proposed spring-based metamaterials, highlighting their potential applications in energy absorption and soft robotics.

4. Conclusions

In this study, we proposed a novel class of flexible mechanical metamaterials based on spring elements. These spring elements exhibit superior resilience and reversibility, demonstrably facilitating the rapid recovery of the metamaterials even after large deformation, as experimentally validated up to 10% compressive strain. A significant advantage of discretely assembling these spring elements into a metamaterial is the circumvention of fabrication limitations and the potential for low-cost production. Notably, the design process is accelerated through deep learning frameworks, which not only predict effective mechanical properties from design parameters but also empower the inverse design of metamaterials to meet specified target properties. This approach yields comprehensive contour maps delineating Young's moduli and Poisson's ratios across a wide range of property space. Importantly, the deep learning models demonstrate zero-shot learning capabilities, thus facilitating the generation of designs with properties that extend beyond the bounds of the original training data.

The inverse design capability proves exceptionally valuable for applications requiring precise property manipulation, notably in energy absorption systems and soft robotics. The adaptable nature of this deep learning-accelerated design framework implies its extensibility to a wider range of metamaterial architectures, potentially integrating diverse geometric representations, including voxels, point clouds, and meshes. Although our current work is centered on a specific class of metamaterials and constrained to three trained lattice configurations (SC, BCC, and FCC), it presents a compelling challenge to traditional forward design paradigms. In contrast to the conventional approach of property determination after geometry definition, our approach proposes an interactive co-design paradigm wherein properties, geometries, and material compositions are concurrently engineered. The integration of advanced deep generative models and large language models promises to further amplify this capability, ultimately paving the way

for fully automated, highly versatile, and application-centric metamaterial design strategies.

CRediT authorship contribution statement

Xiaofeng Guo: Writing – original draft, Visualization, Validation, Methodology, Investigation, Formal analysis, Data curation. **Xiaoyang Zheng:** Writing – original draft, Visualization, Validation, Methodology, Investigation, Formal analysis, Data curation, Conceptualization. **Jiaxin Zhou:** Validation, Investigation. **Takayuki Yamada:** Resources. **Yong Yi:** Supervision. **Ikumu Watanabe:** Writing – review & editing, Writing – original draft, Supervision, Software, Resources, Project administration, Methodology, Conceptualization.

Declaration of competing interest

The authors declare that they have no known competing financial interests or personal relationships that could have appeared to influence the work reported in this paper.

Acknowledgements

This study was partly supported by the Japan Science and Technology Agency – Supporting Program for Innovative Research on Cutting-Edge Science and Technology (SPRING), Grant Number JPMJSP2124. X. Guo acknowledges the NIMS Internship Program for the stay and research in Japan.

Data availability

Data will be made available on request.

References

[1] X. Zheng, X. Zhang, T.-T. Chen, I. Watanabe, Deep learning in mechanical metamaterials: from prediction and generation to inverse design, Adv. Mater. 35 (45) (2023) 2302530.
[2] P. Jiao, J. Mueller, J.R. Raney, X. Zheng, A.H. Alavi, Mechanical metamaterials and beyond, Nat. Commun. 14 (1) (2023) 6004.
[3] D. Akamatsu, Y. Noguchi, K. Matsushima, Y. Sato, J. Yanagimoto, T. Yamada, Two-phase topology optimization for metamaterials with negative Poisson's ratio, Compos. Struct. 311 (2023) 116800.
[4] X. Ren, R. Das, P. Tran, T.D. Ngo, Y.M. Xie, Auxetic metamaterials and structures: a review, Smart Mater. Struct. 27 (2) (2018) 023001.
[5] X. Zheng, X. Guo, I. Watanabe, A mathematically defined 3d auxetic metamaterial with tunable mechanical and conduction properties, Mater. Des. 198 (2021) 109313.
[6] T.A. Schaedler, A.J. Jacobsen, A. Torrents, A.E. Sorensen, J. Lian, J.R. Greer, L. Valdevit, W.B. Carter, Ultralight metallic microlattices, Science 334 (6058) (2011) 962–965.
[7] B. Chen, L. Chen, B. Du, H. Liu, W. Li, D. Fang, Novel multifunctional negative stiffness mechanical metamaterial structure: tailored functions of multi-stable and compressive mono-stable, Composites, Part B, Eng. 204 (2021) 108501.
[8] T. Hewage, K. Alderson, A. Alderson, F. Scarpa, Double-negative mechanical metamaterials displaying simultaneous negative stiffness and negative Poisson's ratio properties, Adv. Mater. 28 (46) (2016) 10323–10332.
[9] X. Zheng, I. Watanabe, S. Wang, T.-T. Chen, M. Naito, Minimal-surface-based multiphase metamaterials with highly variable stiffness, Mater. Des. 237 (2024) 112548.
[10] C.B. Churchill, D.W. Shahan, S.P. Smith, A.C. Keefe, G.P. McKnight, Dynamically variable negative stiffness structures, Sci. Adv. 2 (2) (2016) e1500778.
[11] T. Chen, M. Pauly, P.M. Reis, A reprogrammable mechanical metamaterial with stable memory, Nature 589 (7842) (2021) 386–390.
[12] X. Zheng, K. Uto, W.-H. Hu, T.-T. Chen, M. Naito, I. Watanabe, Reprogrammable flexible mechanical metamaterials, Appl. Mater. Today 29 (2022) 101662.
[13] S. Pyo, K. Park, Mechanical metamaterials for sensor and actuator applications, Int. J. Precis. Eng. Manuf.-Green Technol. 11 (1) (2024) 291–320.
[14] K.K. Dudek, J.A. Iglesias Martínez, G. Ulliac, L. Hirsinger, L. Wang, V. Laude, M. Kadic, Micro-scale mechanical metamaterial with a controllable transition in the Poisson's ratio and band gap formation, Adv. Mater. 35 (20) (2023) 2210993.
[15] J. Wu, Y. Zhang, F. Yang, F. Jiang, X. Xu, Y. Tan, L. Su, A hybrid architectural metamaterial combing plate lattice and hollow-truss lattice with advanced mechanical performances, Addit. Manuf. 76 (2023) 103764.
[16] S. Tomita, K. Shimanuki, H. Nishigaki, S. Oyama, T. Sasagawa, D. Murai, K. Umemoto, Origami-inspired metamaterials with switchable energy absorption based on bifurcated motions of a Tachi-Miura polyhedron, Mater. Des. 225 (2023) 111497.
[17] X. Xin, L. Liu, Y. Liu, J. Leng, 4d pixel mechanical metamaterials with programmable and reconfigurable properties, Adv. Funct. Mater. 32 (6) (2022) 2107795.
[18] C. Coulais, E. Teomy, K. De Reus, Y. Shokef, M. Van Hecke, Combinatorial design of textured mechanical metamaterials, Nature 535 (7613) (2016) 529–532.
[19] K. Bertoldi, V. Vitelli, J. Christensen, M. Van Hecke, Flexible mechanical metamaterials, Nat. Rev. Mater. 2 (11) (2017) 1–11.
[20] M. Pishvar, R.L. Harne, Foundations for soft, smart matter by active mechanical metamaterials, Adv. Sci. 7 (18) (2020) 2001384.
[21] X.C. Teng, X. Ren, Y. Zhang, W. Jiang, Y. Pan, X.G. Zhang, X.Y. Zhang, Y.M. Xie, A simple 3d re-entrant auxetic metamaterial with enhanced energy absorption, Int. J. Mech. Sci. 229 (2022) 107524.
[22] A.G. Mark, S. Palagi, T. Qiu, P. Fischer, Auxetic metamaterial simplifies soft robot design, in: 2016 IEEE International Conference on Robotics and Automation (ICRA), IEEE, 2016, pp. 4951–4956.
[23] S. Bonfanti, R. Guerra, F. Font-Clos, D. Rayneau-Kirkhope, S. Zapperi, Automatic design of mechanical metamaterial actuators, Nat. Commun. 11 (1) (2020) 4162.
[24] S.C. Han, D.S. Kang, K. Kang, Two nature-mimicking auxetic materials with potential for high energy absorption, Mater. Today 26 (2019) 30–39.
[25] M. Askari, D.A. Hutchins, P.J. Thomas, L. Astolfi, R.L. Watson, M. Abdi, M. Ricci, S. Laureti, L. Nie, S. Freear, et al., Additive manufacturing of metamaterials: a review, Addit. Manuf. 36 (2020) 101562.
[26] J. Fan, L. Zhang, S. Wei, Z. Zhang, S.-K. Choi, B. Song, Y. Shi, A review of additive manufacturing of metamaterials and developing trends, Mater. Today 50 (2021) 303–328.
[27] A. Nazir, O. Gokcekaya, K.M.M. Billah, O. Ertugrul, J. Jiang, J. Sun, S. Hussain, Multi-material additive manufacturing: a systematic review of design, properties, applications, challenges, and 3d printing of materials and cellular metamaterials, Mater. Des. 226 (2023) 111661.
[28] Y. Huang, T.G. Fleming, S.J. Clark, S. Marussi, K. Fezzaa, J. Thiyagalingam, C.L.A. Leung, P.D. Lee, Keyhole fluctuation and pore formation mechanisms during laser powder bed fusion additive manufacturing, Nat. Commun. 13 (1) (2022) 1170.
[29] B. Jenett, C. Cameron, F. Tourlomousis, A.P. Rubio, M. Ochalek, N. Gershenfeld, Discretely assembled mechanical metamaterials, Sci. Adv. 6 (47) (2020) eabc9943.
[30] J.P. Lang, W. Jiang, X.C. Teng, X.G. Zhang, D. Han, J. Hao, H.H. Xu, X.H. Ni, Y.M. Xie, Q.H. Qin, et al., Assembled mechanical metamaterials with transformable shape and auxeticity, Constr. Build. Mater. 378 (2023) 131181.
[31] J. He, Y. Wang, Z. Shen, L. Xia, Y. Xiong, Assembled mechanical metamaterials with integrated functionalities of programmable multistability and multitransition behaviors, Mater. Horiz. (2024).
[32] C.E. Gregg, D. Catanoso, O.I.B. Formoso, I. Kostitsyna, M.E. Ochalek, T.J. Olatunde, I.W. Park, F.M. Sebastianelli, E.M. Taylor, G.T. Trinh, et al., Ultralight, strong, and self-reprogrammable mechanical metamaterials, Sci. Robot. 9 (86) (2024), eadi2746.
[33] C.H. Belke, J. Paik, Mori: a modular origami robot, IEEE/ASME Trans. Mechatron. 22 (5) (2017) 2153–2164.
[34] C.H. Belke, K. Holdcroft, A. Sigrist, J. Paik, Morphological flexibility in robotic systems through physical polygon meshing, Nat. Mach. Intell. 5 (6) (2023) 669–675.
[35] D. Lee, W. Chen, L. Wang, Y.-C. Chan, W. Chen, Data-driven design for metamaterials and multiscale systems: a review, Adv. Mater. 36 (8) (2024) 2305254.
[36] J.-H. Bastek, S. Kumar, B. Telgen, R.N. Glaesener, D.M. Kochmann, Inverting the structure–property map of truss metamaterials by deep learning, Proc. Natl. Acad. Sci. 119 (1) (2022) e2111505119.
[37] X. Zheng, I. Watanabe, J. Paik, J. Li, X. Guo, M. Naito, Text-to-microstructure generation using generative deep learning, Small (2024) 2402685.
[38] Y. Mao, Q. He, X. Zhao, Designing complex architectured materials with generative adversarial networks, Sci. Adv. 6 (17) (2020) eaaz4169.
[39] H.T. Kollmann, D.W. Abueidda, S. Koric, E. Guleryuz, N.A. Sobh, Deep learning for topology optimization of 2d metamaterials, Mater. Des. 196 (2020) 109098.
[40] X. Zheng, T.-T. Chen, X. Guo, S. Samitsu, I. Watanabe, Controllable inverse design of auxetic metamaterials using deep learning, Mater. Des. 211 (2021) 110178.
[41] X. Zheng, T.-T. Chen, X. Jiang, M. Naito, I. Watanabe, Deep-learning-based inverse design of three-dimensional architected cellular materials with the target porosity and stiffness using voxelized Voronoi lattices, Sci. Technol. Adv. Mater. 24 (1) (2023) 2157682.
[42] G. Oliveri, J.T. Overvelde, Inverse design of mechanical metamaterials that undergo buckling, Adv. Funct. Mater. 30 (12) (2020) 1909033.
[43] S. Kumar, S. Tan, L. Zheng, D.M. Kochmann, Inverse-designed spinodoid metamaterials, npj Comput. Mater. 6 (1) (2020) 73.
[44] C.S. Ha, D. Yao, Z. Xu, C. Liu, H. Liu, D. Elkins, M. Kile, V. Deshpande, Z. Kong, M. Bauchy, et al., Rapid inverse design of metamaterials based on prescribed mechanical behavior through machine learning, Nat. Commun. 14 (1) (2023) 5765.
[45] I. Watanabe, A. Yamanaka, Voxel coarsening approach on image-based finite element modeling of representative volume element, Int. J. Mech. Sci. 150 (2019) 314–321.
[46] I. Watanabe, D. Setoyama, N. Nagasako, N. Iwata, K. Nakanishi, Multiscale prediction of mechanical behavior of ferrite–pearlite steel with numerical material testing, Int. J. Numer. Methods Eng. 89 (7) (2012) 829–845.